# Flow and heat transfer characteristics of air compression in a liquid piston for compressed air energy storage

El Mehdi Gouda, Mustapha Benaouicha, Thibault Neu, Yilin Fan, Lingai Luo

▶ **To cite this version:**

El Mehdi Gouda, Mustapha Benaouicha, Thibault Neu, Yilin Fan, Lingai Luo. Flow and heat transfer characteristics of air compression in a liquid piston for compressed air energy storage. Energy, 2022, 254, pp.124305. 10.1016/j.energy.2022.124305 . hal-03690959

**HAL Id: hal-03690959**
**https://hal.science/hal-03690959**

Submitted on 8 Jun 2022

**HAL** is a multi-disciplinary open access archive for the deposit and dissemination of scientific research documents, whether they are published or not. The documents may come from teaching and research institutions in France or abroad, or from public or private research centers.

L'archive ouverte pluridisciplinaire **HAL**, est destinée au dépôt et à la diffusion de documents scientifiques de niveau recherche, publiés ou non, émanant des établissements d'enseignement et de recherche français ou étrangers, des laboratoires publics ou privés.

# Flow and heat transfer characteristics of air compression in a liquid piston for compressed air energy storage

El Mehdi GOUDA[a,b], Mustapha BENAOUICHA[a,*], Thibault NEU[a], Yilin FAN[b], Lingai LUO[b,*]

[a] *Segula Technologies. Naval and Energy Engineering Research and Innovation Unit. 9 avenue Edouard Belin, 92500 Rueil-Malmaison, France*
[b] *Nantes Université, CNRS, Laboratoire de Thermique et Énergie de Nantes, LTeN, UMR 6607, F-44000 Nantes, France*

**Abstract**

The breakthrough in energy storage technology is the key issue for the renewable energy penetration and compressed air energy storage (CAES) has demonstrated the potential for large-scale energy storage of power plants. Liquid piston (LP) technology has been developed to achieve the Isothermal CAES with improved efficiency, but the description and the physical understanding of the coupled flow and heat transfer dynamic behaviors are lacking. In this study, a 3D CFD model for LP compressor using finite-volume method and VOF method is developed and validated by the existing experimental data-sets. The air compression in the LP column is simulated and air flow and temperature characteristics are obtained and analyzed in detail for the first time. Results clearly show the existence of different flow patterns over the compression time. The establishment of axisymmetric flow structure, its evolution and transition to totally chaotic one can be identified. The instabilities due to the high shear stress and frictions at the interface between the central-ascending & peripheral-descending streams may cause this flow structure disruption. The air temperature rise (32.5 K) at the end of compression is 7.7 times smaller than that of adiabatic

*DOI:* `https://doi.org/10.1016/J.ENERGY.2022.124305`
*Corresponding author
*Email addresses:* `mustapha.benaouicha@segula.fr` (Mustapha BENAOUICHA), `lingai.luo@univ-nantes.fr` (Lingai LUO)

operation, confirming the interests of LP in realizing Isothermal-CAES systems.

*Keywords:* Compressed air energy storage (CAES); Liquid Piston (LP); Air compression; Flow regime; VOF method; Heat transfer

---

**Nomenclature**

**Abbreviations**

| | |
|---|---|
| CAES | Compressed Air Energy Storage |
| CFD | Computational Fluid Dynamics |
| CR | Compression Ratio |
| ESS | Energy Storage System |
| Exp. | Experimental |
| FVM | Finite Volume Method |
| I-CAES | Isothermal Compressed Air Energy Storage |
| LES | Large Eddy Simulation |
| LP | Liquid Piston |
| Num. | Numerical |
| PIV | Particle Image Velocimetry |
| RTE | Round Trip Efficiency |
| VOF | Volume Of Fluid |

**Greek Symbols**

| | |
|---|---|
| $\alpha$ | Volume fraction |
| $\lambda$ | Thermal conductivity ($Wm^{-1}K^{-1}$) |

$\mu$ Dynamic viscosity ($kg\,m^{-1}s^{-1}$)

$\nu$ Kinematic viscosity ($m^2s^{-1}$)

$\rho$ Density ($kg\,m^{-3}$)

$\sigma$ Surface tension coefficient ($Nm^{-1}$)

**Non-dimensional numbers**

$Co$ Courant number

$Nu$ Nusselt number

$Pr$ Prandtl number

$Re$ Reynolds number

**Latin symbols**

$c$ Heat capacity ($JK^{-1}kg^{-1}$)

$D$ Diameter ($m$)

$e$ Energy ($J$)

$g$ Gravitational acceleration ($ms^{-2}$)

$L$ Length ($m$)

$m$ Mass ($kg$)

$P$ Pressure ($Pa$)

$Q$ Flow rate ($m^3s^{-1}$)

$R$ Radius ($ms^{-2}$)

$r$ Specific gas constant ($JKg^{-1}K^{-1}$)

$T$ Temperature ($K$)

$t$ Time ($s$)

$U$ Velocity ($ms^{-1}$)

$V$ Volume ($m^3$)

**Subscripts**

$air$ Air

$f$ Final at $t = t_f$

$ini$ Initial at $t = 0$ s

$interface$ Water/Air interface

$k$ Kinematic

$liquid$ Liquid

$pist$ Piston

$walls$ Wall

$water$ Water

## 1. Introduction

Renewable energy sources (e.g., wind, solar, tidal) has significantly increased their share in global electricity generation in recent years, reaching almost 29% (8300 TWh) in 2020 [1]. To overcome their intrinsic intermittent character, the development and application of efficient energy storage technologies are specially required, aiming at improving the reliability and dispatchability of the power plants driven by these renewable sources [2, 3]. Moreover, the integration of energy storage systems (ESSs) in the distribution network and their exploitation in the smart grid context could better balance the electricity production and consumption, accelerating the pathway to a flexible, low-cost and electrified future [4, 5].

Among various energy storage technologies, the Compressed Air Energy Storage (CAES) is shown to be one of the most promising and cost-effective

methods for electricity storage at large-scale [6], owing to its high storage capacity, low self-discharge, and long lifetime [7]. Surplus electricity power could be stored by compressing and storing air (or another gas) in man-made containers or natural caverns in the form of elastic potential energy. The electricity could be restituted through a turbine by expanding the compressed air during high power demand period [8, 9, 10]. CAES facilities have already been commercialized and are expected to capture a bigger market share of ESS in a near future [10].

One of the major problems of conventional CAES systems is the air temperature rise or fall during the compression or expansion operation, respectively, resulting in the low round trip efficiency (RTE). Therefore, the new generation of CAES technology seeks to approach the isothermal cyclic operations (I-CAES) by efficient thermal management of heat release and supply [11, 12]. To achieve this goal, the liquid piston (LP) concept has been proposed as an alternative to conventional solid piston machinery [13]. This concept is featured by the use of a slender column where a liquid (often water) is used to increase or decrease the pressure of a gas (often air). The large heat capacity of water and the greater air/wall contact surface area due to the high length/diameter ratio ($\frac{L}{D} >> 1$) of the LP column favor the heat exchanges between the air and the environment. Moreover, the air leakage and the friction dissipation could be largely reduced [14, 13], leading to higher compression/expansion efficiencies. The study of Van de Ven & Li [13] showed that 19% decrease in energy consumption and 13% increase in compression efficiency could be achieved by the LP compressor compared to the conventional solid piston. Recent CAES projects such as REMORA developed by Segula Technologies [15, 16] and GLIDES by Oak Ridge National Laboratory [17] also reported that up to 95% compressor/expander efficiency could be achieved by LP, demonstrating the great interest in the development and deployment of this technology for I-CAES. The power output for a single LP column for industrial application could reach 1 kW and further increase of power output is achievable by installing a number of LP columns in parallel sequencing mode, e.g., 6 MW for REMORA [16].

Subsequently, a large number of studies have been performed to better characterize the compression/expansion processes using the LP, as summarized in the recent review paper of Gouda et al. [12]. Some studies were based on the thermodynamic analysis of the compression/expansion operation, investigating the influences of geometric parameters [18, 14], operating conditions [19, 17] or working couples [19, 20] on the compression/expansion efficiency of the LP column. Others tried to propose and implement thermal management measures for heat transfer enhancement [21, 22, 23], so as to better approach the isothermal cycle. Commonly, the global temperature and pressure evolution of the gas phase was experimentally measured and monitored. The obtained data were used to develop heat transfer models and to calculate the efficiency. Relatively fewer studies were devoted to the characterization of fluid flow patterns and heat transfer behaviors at local level using different numerical and/or experimental methods. Some of these studies for the compression process are listed in Table 1.

Most of the previous numerical studies were limited to 2D domain [24, 25], for the purpose of reducing the computational cost compared to 3D full simulation. For example, by using a 2D axisymmetric computational fluid dynamics (CFD) model, Zhang et al. [25, 26] showed that higher Reynolds number at high piston speed would result in the lower heat transfer rate during the compression process and thus the lower compression efficiency. Similar tendency was also reported by Coetzee et al. [27] by applying the moving boundary of a solid piston in a 2D axisymmetric CFD model. Mutlu & Kiliç [28] showed that the compression efficiency decreased with the increasing piston speed, especially at high compression ratio (CR) and high $L/D$ ratio of the LP column. Nevertheless, the 2D simplification brings difficulties in correctly simulating the thermohydrodynamic behaviors of the gas flow by ignoring the 3D nature of flow structure and local turbulence [24]. Moreover, the heat exchange between the walls and the fluids would be underestimated due to the doubled compactness ratio of 2D geometry with respect to 3D, which in turn modifies the air flow behaviors [29]. The necessity of 3D simulation for air compression by LP

is thereby highlighted despite the higher computational cost [30, 31]. Noteworthy is the work of Zhang et al. [32] who first performed 3D CFD simulations of a LP compressor applied to CAES using the Volume of Fluid (VOF) model. Later, a geometric optimization study by Zhang et al. [18] using 3D VOF model showed that a gourd-shaped LP compressor favored the heat transfer. Nevertheless, their works have been focused on finding new Nusselt number correlations to model the heat transfer inside the LP by monitoring the evolution of gas temperature.

Currently the experimental characterization of the air flow and temperature evolution at local level is very rare, which may be attributed to the difficulty in implementing proper measuring techniques that have limited influence on the flow pattern. Wieberdink et al. [23] experimentally tested the effect of different porous inserts in a LP column subjected to different compression/expansion speeds at high pressure ($2.1 \times 10^7\, Pa$). Patil et al. [21] experimentally investigated the heat transfer in a LP compressor with different compression chamber's materials. Four thermocouples were used to measure the local temperature evolution inside the LP column, but insufficient to correctly construct the temperature field during compression/expansion processes. In a very recent study, Li et al. [33] experimentally tested a pilote-scale LP ($L$=6.5 m; $D$=2.2 m; $V$=24.71 $m^3$) at very slow piston speed ($4 \times 10^{-4}$ to $1 \times 10^{-3}\, m.s^{-1}$) and a small air temperature variation (11 K). In their study, 5 temperature sensors have been implemented to monitor the axial temperature variations and to quantify the heat transfer rate during the compression/expansion operations. In the existing literature, the only experimental study that provides quantitative information on the air velocity field and its evolution has been performed by Neu & Subrenat [34]. A specially designed solid piston has been used to approximately represent the concept of LP and the air flow inside has been visualized by the Particle Image Velocimetry (PIV) technique. While this valuable data-set on the velocity fields has been used for the model validation of the present study, no further information on the local temperature profile could be derived from their study.

| Study | Year | Type | $L/D$ | CR | Working fluids | Methodology | Main findings | Notes |
|---|---|---|---|---|---|---|---|---|
| Van de Ven & Li [13] | 2009 | Num. + Exp. | 44 | 9.5 | Air/water | Simplified numerical model<br>$Re_{liquid} = 300$ | 100 K air temperature<br>increase | 50000 small<br>cylinder inserts |
| Piya et al. [35] | 2009 | Num. | 26.2-130 | 9.8 | Air & Helium/<br>Water & DTE 25 | $89 < Re < 4800$ for liquid<br>$Re = 350$ for gas<br>Energy balance equation | Better efficiency with<br>Helium/water combination | Comparison of 5<br>chamber diameters |
| Zhang et al. [26, 36] | 2013 | Num. + Exp. | 6.9 | 10 | Air/water | 2D CFD, test of a 0-D model<br>+ comparison to experiments | New $Nu$ correlation proposed;<br>validation of the 0-D model | Interrupted plate;<br>metal-foam inserts |
| Zhang et al. [32, 37] | 2014 | Num. | 11.5 | 11-22 | Air/water | 3D CFD<br>VOF method with LES model<br>$500 < Re < 2000$ | New $Nu$ correlation proposed | Porous media<br>inserts |
| Qin & Loth [38] | 2014 | Num. + Exp. | 1 | 6-12 | Air/water | Thermodynamic analysis<br>+ 1D model | Validated numerical<br>model by experiments | Spray injection |
| Coetzee et al. [27] | 2016 | Num. + Exp. | 52 | 2 | Air/solid piston | 2D axisymmetric CFD;<br>moving boundary of interface | Decreased heat transfer with<br>increasing piston speed | Local and average<br>temperature evolution |
| Zhang et al. [18] | 2016 | Num. | 30 | 30 | Air/water | 3D CFD, VOF method | Best performance achieved<br>by a gourd-shaped LP | Shape optimization of<br>the piston column |
| Wieberdink et al. [23] | 2018 | Exp. | 6.35 | 30 | Air/water | Inverse method | Effects of geometry and<br>position of the inserts<br>on the efficiency evaluated | Porous media;<br>compression & expansion |
| Patil et al. [21] | 2019 | Exp. | 1.2-1.94 | 2.05-2.35 | Air/water | Local temperature<br>measurement by thermocouples | Effect of piston wall<br>materials evaluated | Spray injection |
| Gouda et al. [24] | 2019 | Num. | 50 | 4 | Air/water | 2D CFD;<br>VOF method+LES turbulence model | Flow regime transition studied | Comparison with experimental<br>results from [14] |
| Neu et al. [14] | 2020 | Exp. | 20-180 | 4-8 | Air/water | Local temperature<br>measurement + inverse method | New $Nu$ correlations and<br>flow regime transition criteria proposed | Different LP sizes |
| Neu & Subrenat [34] | 2021 | Exp. | 35 | 5 | Air/solid piston | PIV | Air flow inside<br>piston visualized during slow<br>compression | Results used for<br>comparison and validation of<br>the present numerical model |
| Li et al. [33] | 2022 | Exp. | 3 | 1.8-10 | Air/water | Local temperature measurement<br>by 5 temperature detectors | Quantification of<br>heat transfer rate | Very slow piston speed<br>Pilote scale LP |
| Zhou et al. [39] | 2022 | Num. | 0.6 | 2.25 | Ionic fluids/<br>hydrogen | 3D CFD | New correlations<br>for pressure drop and $Nu$ | Porous media<br>inserts |

Table 1: Some experimental and numerical studies on the local air thermohydrodynamic behaviors inside the LP (or solid) compressor

From the above literature survey, it can be seen that the research gap still exists on the detailed analysis of the conjugated fluid flow and heat transfer inside the LP column during compression or expansion operation. In particular, systematic studies that quantitatively characterize local air velocity profiles and temperature fields are still lacking. As a result, the fluid flow dynamics inside the LP column, the evolution and transition between different flow patterns and their effects on the heat transfer are far from clear. Hence, the main objective of the present study is to characterize and understand the evolution of air/water flow patterns and the conjugated heat transfer inside the LP compressor through numerical modeling and simulation. To do this, a numerical model based on Finite Volume Method (FVM) coupled with the VOF method for water/air interface tracking was firstly developed and validated by the data-set of Neu & Subrenat [34]. Then, 3D dynamic simulations were performed to obtain detailed air velocity and temperature fields and their evolution during different stages of the compression process. The flow patterns and their transition were analysed in detail in order to achieve a better understanding of the associated physical phenomena, i.e., the origin of the flow structure disruption.

The contribution of the current work is important because it will expand the limited knowledge by providing, for the first time, such detailed local fluid flow and heat transfer characteristics in a LP compressor. The obtained results will allow better understanding of the flow and heat transfer mechanisms on one hand, and the development of appropriate analytical physical models for performance description and prediction of LP operations on the other hand. Moreover, the perspective exploitation of the obtained results would help identify performance improvement pathways for the development of highly-efficient Isothermal-CAES systems with the potential of their large-scale application in various industrial sectors.

## 2. Methodology

### *2.1. Geometry of the LP column and basic assumptions*

The physical phenomena occurred inside a LP compressor is rather complex, involving the gas-liquid two-phase flow at transient-state with heat transfer at relatively low Reynolds and Mach numbers. Initially at rest the air is set as motionless, but then compressed by the advancement of the liquid front. Several flow patterns (one following another) may occur along with the piston advancement, as has been reported in the literature [40, 24, 26] and will be further discussed in the following sections of this study.

The LP configuration and operating conditions numerically studied here are based on the experimental setup used by Neu & Subrenat [34], both within the framework of the REMORA project [15, 16]. The reason is to validate the numerical model by the available experimental data-set through the results comparison. Note that in experiments, a solid piston has been used to replace the LP operation to avoid the technical problems of PIV measurement. The column has been specially designed, i.e., with a large $L/D$ ratio and a slow compression speed, so that the air flow behavior inside can be considered as identical to that of the LP. The physical model of the compression chamber, as shown in Fig. 1, involves a vertical and elongated cylinder with a diameter $D = 0.0518$ m and a length $L_{ini} = 0.906$ m. The length to diameter ratio being thus $L/D = 17.5$. The column is initially filled with air (as the gas phase), and water (as the liquid phase) is then injected at the bottom surface. The lateral and top surfaces of the column are considered as closed walls.

The following general assumptions are made in the numerical model:

- The compressed gas (air) is considered as ideal gas;
- The liquid phase (water) is considered as incompressible flow;
- Uniform and constant temperature at the walls with zero thickness;
- No phase change occurs for the working fluids;
- No mass transfer occurs between water and air.

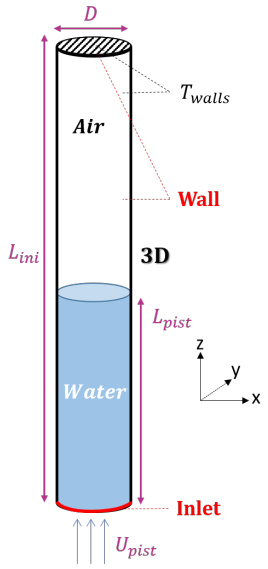


Figure 1: The studied LP geometry and boundaries

### *2.2. VOF method for air compression with heat transfer*

The main challenge in simulating multi-phase flow is the use of appropriate method to handle the change of fluid properties across the interface. In this study, FVM was used to solve the Navier-Stokes equations coupled with the VOF method for the interface tracking. This method can describe the location of two immiscible fluids by solving a single set of conservative equations and by tracking the volume fraction of each fluid [41]. It is one of the most powerful and robust tools capable of handling multi-phase flow with a high density ratio, e.g., as high as 1000 for the case of water and air inside the LP column. In fact, for a stratified compressible multi-phase flow, the VOF method has been reported to have the best stability with a reasonable computational cost [42]. Moreover, the interface diffusion phenomenon, as a common problem that may be encountered by using the VOF method, is limited in our study since in the slender LP column, the water/air interface is generally flat and occupies a very small volume compared to the volume of each phase.

The volume fraction of the water component in a cell of the computational

grid is given by Eq. 1:

$$\alpha = \frac{V_{water}}{V_{cell}} \tag{1}$$

Where $V_{water}$ is the volume of water.

The density $\rho$ and the viscosity $\mu$ of mixture are given by Eq. 2 and Eq. 3, respectively:

$$\rho = \alpha\rho_{water} + (1-\alpha)\rho_{air} \tag{2}$$

$$\mu = \alpha\mu_{water} + (1-\alpha)\mu_{air} \tag{3}$$

The mass conservation equation is given by:

$$\frac{\partial \rho}{\partial t} + \nabla \cdot (\rho \mathbf{U}) = 0 \tag{4}$$

where $\mathbf{U}$ represents the velocity vector.

The momentum conservation equation is given by :

$$\frac{\partial \rho \mathbf{U}}{\partial t} + \nabla \cdot (\rho \mathbf{U}\mathbf{U}) - \nabla \cdot (\mu \nabla \mathbf{U}) = \sigma\kappa\nabla\alpha - \mathbf{g} \cdot \mathbf{x}\nabla\rho - \nabla P_d \tag{5}$$

where $\sigma$ is the surface tension coefficient; the curvature of the interface is calculated as $\kappa = \nabla \cdot \frac{\nabla\alpha}{|\nabla\alpha|}$; $P_d = P - \rho\mathbf{g} \cdot \mathbf{x}$ is the dynamic pressure; $\mathbf{g}$ is the gravitational acceleration and $\mathbf{x}$ is the position vector.

The energy equation is given by:

$$\frac{\partial \rho T}{\partial t} + \nabla \cdot (\rho \mathbf{U} T) - \nabla \cdot (\mu \nabla T) = -\left(\frac{\alpha}{c_{v,water}} + \frac{1-\alpha}{c_{v,air}}\right)\left(\frac{\partial \rho e_k}{\partial t} + \nabla \cdot (\mathbf{U} e_k) - \nabla \cdot (\mathbf{U} P)\right) \tag{6}$$

where $e_k = \frac{|\mathbf{U}|^2}{2}$ is the specific kinetic energy; $c_{v,water}$ and $c_{v,air}$ are the specific heat capacity at constant volume for the water and air phase, respectively.

A transport equation for the water volume fraction used to capture the free surface is given by:

$$\frac{\partial \alpha}{\partial t} + \mathbf{U} \cdot \nabla\alpha + \nabla \cdot \mathbf{U_r}\alpha(1-\alpha) = 0 \tag{7}$$

where $\nabla \cdot \mathbf{U_r}\alpha(1-\alpha)$ is an anti-diffusion term utilised to sharpen the interface and $\mathbf{U}_r = \mathbf{U}_{water} - \mathbf{U}_{air}$ is the relative velocity vector, designated as the "compression velocity".

*2.3. Simulation parameters*

The transport equations of mass, momentum and energy were closed by the equations of state for density and enthalpy. The ideal gas law (Eq. 8) was used to model the air since in this study the air temperature didn't exceed 400 K and the maximum pressure was $5 \times P_{atm}$.

$$\rho = \frac{1}{rT} P \tag{8}$$

The Sutherland equation (Eq. 9) was used for the temperature-dependent viscosity of air:

$$\mu(T) = \mu_0 \frac{T_0 + C}{T + C} \left( \frac{T}{T_0} \right)^{\frac{3}{2}} \tag{9}$$

where $C = 110.4$ is the Sutherland coefficient, $T_0 = 273.15$ K is the reference temperature and $\mu_0 = 18.27 \cdot 10^{-6}$ Pa.s is the reference viscosity. Constant thermal conductivity $\lambda_{air}$ and heat capacity of air $c_{v,air}$ at 293 K and $1 \times 10^5$ Pa were used in the simulation (Table 2). For the water phase with almost no temperature change during compression, constant physical properties at 293 K and $1 \times 10^5$ Pa were used. These values are listed in Table 3.

| | Initial state $T$=293 K $P = 10^5 Pa$ | Final state $T$=400 K $P = 5.5 \times 10^5 Pa$ | Units | Relative difference |
|---|---|---|---|---|
| $\mu_{air}$ | $1.836 \times 10^{-5}$ | $2.326 \times 10^{-5}$ | $kg.m^{-1}.s^{-1}$ | 26.7% |
| $\lambda_{air}$ | $2.587 \times 10^{-2}$ | $2.95 \times 10^{-2}$ | $W.m^{-1}.K^{-1}$ | 10.2% |
| $c_{p_{air}}$ | $1.0068 \times 10^3$ | $1.0181 \times 10^3$ | $J.kg^{-1}.K^{-1}$ | 1.1% |

Table 2: Physical properties of air used in the simulation

OpenFOAM code (version 7) with the *CompressibleInterFoam* solver [43] was used to solve the governing equations. A fixed value of water velocity at 0.033 $ms^{-1}$ was imposed at the inlet boundary while all the other boundaries were treated as isothermal no-slip walls (Fig. 1). This piston speed is identical to that tested in the previous experimental study [34] for easy comparison and

| | Initial state $T$=293 K $P = 10^5 Pa$ | Final state $T$=293 K $P = 5.5 \times 10^5 Pa$ | Units | Relative difference |
|---|---|---|---|---|
| $\mu_{water}$ | $1.007 \times 10^{-3}$ | $1.005 \times 10^{-3}$ | $kg.m^{-1}.s^{-1}$ | 0.2% |
| $\lambda_{water}$ | $5.98 \times 10^{-1}$ | $5.78 \times 10^{-1}$ | $W.m^{-1}.K^{-1}$ | 3.1% |
| $c_{p_{water}}$ | $4.185 \times 10^3$ | $4.184 \times 10^3$ | $J.kg^{-1}.K^{-1}$ | 0.02% |

Table 3: Physical properties of water used in the simulation

model validation. The influence of piston speed on the air temperature evolution will be further discussed in section 4.3. Detailed initial and boundary conditions for the simulation are listed in Table 4.

| Variables | Initial condition | Boundary conditions | |
|---|---|---|---|
| | Full domain | Wall | Inlet |
| $U\ (ms^{-1})$ | $U_x = 10^{-5}$, $U_y = 10^{-5}$, $U_z = 10^{-5}$ | no-slip $U_{walls} = 0$ | Dirichlet $U = U_{pist}$ |
| $P\ (Pa)$ | 101325 | $\frac{\partial P}{\partial n}\|_\Gamma = 0$ | $\frac{\partial P}{\partial n}\|_\Gamma = 0$ |
| $T\ (K)$ | 293 | Dirichlet 293 | Dirichlet 293 |

Table 4: Boundary and initial conditions for the simulation of air compression inside the LP column

The Reynolds number of the water and air (Eqs. 10 and 11), based on the piston speed $U_{pist}$, are calculated to be 1706 and 104, respectively.

$$Re_{water} = \frac{U_{pist} D}{\nu_{water}} = 1706 \tag{10}$$

$$Re_{air} = \frac{U_{pist} D}{\nu_{air}} = 104 \tag{11}$$

Despite the relatively low $Re$ numbers, previous studies in the literature reported the necessity of using a turbulence model to correctly simulate the air

compression by LP [24, 31, 18], mainly because of the existence of vortices induced by the large local air velocities. In this study, the Large Eddy Simulation (LES) with WALE (Wall Adapting Local Eddy-viscosity) as a sub-grid model was employed, suitable for catching and modeling the flow with different regimes it passes through [44].

The PISO algorithm was used for the pressure–velocity coupling in order to ensure an accurate and efficient solution for the unsteady Navier-Stokes equations [45]. Simulations were performed under transient-state with adjusted time step so that the Courant number $Co = \frac{u_i \Delta t}{\delta x}$ was smaller than 1, the condition necessary for the stability of PISO algorithm [46]. Due to the multi-phase flow nature, the interface's Courant number ($Co_{interface}$) as a critical parameter for the calculation stability, is recommended to be smaller than 0.5 [47, 48] . In our study, it was fixed at $Co_{interface} = 0.35$, which controls subsequently the time step of $\Delta t$ varying from $10^{-4}$ s to $10^{-3}$ s.

### *2.4. Dimensionless parameters*

For easier comparison between different LP configurations and operating conditions, some variables and parameters ($T$, $t$, $U$, $P$, $Q$, $L$, $r$) have been normalized to ($T^*$, $t^*$, $U^*$, $P^*$, $Q^*$, $L^*$, $R^*$), as indicated in Table 5.

| Variable | $T$ | $t$ | $U$ | $P$ | $Q$ | $L$ | $r$ |
|---|---|---|---|---|---|---|---|
| Scale | $T_{ini}$ | $t_f$ | $U_{pist}$ | $P_{ini}$ | $Q_{pist}$ | $L_{ini}$ | $R$ |
| Normalized variable | $T^*$ | $t^*$ | $U^*$ | $P^*$ | $Q^*$ | $L^*$ | $R^*$ |

Table 5: Dimensionless parameters and variables

### *2.5. Grid independence study*

A grid independence study has firstly been conducted to determine the appropriate mesh type and size, including hexahedral type mesh ($4.5 \times 10^5$; $9 \times 10^5$ and $1.8 \times 10^6$ elements) and prisms type mesh ($2 \times 10^5$; $6 \times 10^5$ elements). Mesh

comparison was done based on the evolution of average air temperature and pressure during the compression process, especially at the final status when the gradients are relatively high. Simulation results on the evolution of average air temperature (Fig. 3) indicated that the influence of elements number is relatively small, e.g., a maximum difference of less than 1 K between the basic mesh ($4.5 \times 10^5$ elements) and the medium mesh ($9 \times 10^5$ elements), and 0.5 K between the medium and fine mesh ($1.8 \times 10^6$ elements) for the hexahedral mesh. Nevertheless, there is a noticeable difference up to 2 K between the hexahedral and prisms type meshes. The highest velocities observed in the first half of the compression ($t^* < 0.5$) and the transition moment of flow regimes were also checked, showing also a noticeable difference (up to 15%) between these two mesh types. In addition, prism meshes show a later transition and higher final temperature, indicating larger discrepancy with experiments compared to the hexahedral mesh. Hence, the hexahedral mesh (structured O-Grid with refinement at the wall) with $9 \times 10^5$ elements was chosen for the rest of the study (Fig. 2), allowing a relatively faster computing with good accuracy. Good agreement with the experimental data could also be observed by using this mesh, as will be presented in detail in the following subsection.

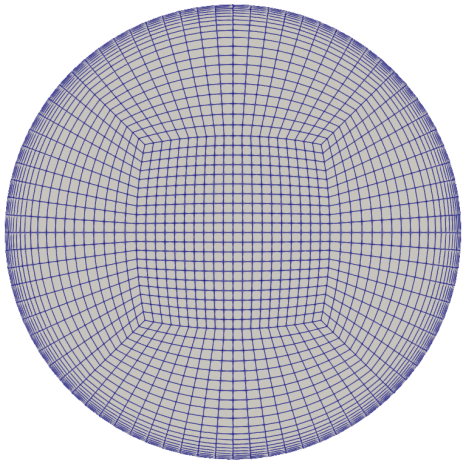

Figure 2: Hexahedral mesh with local refining near the wall

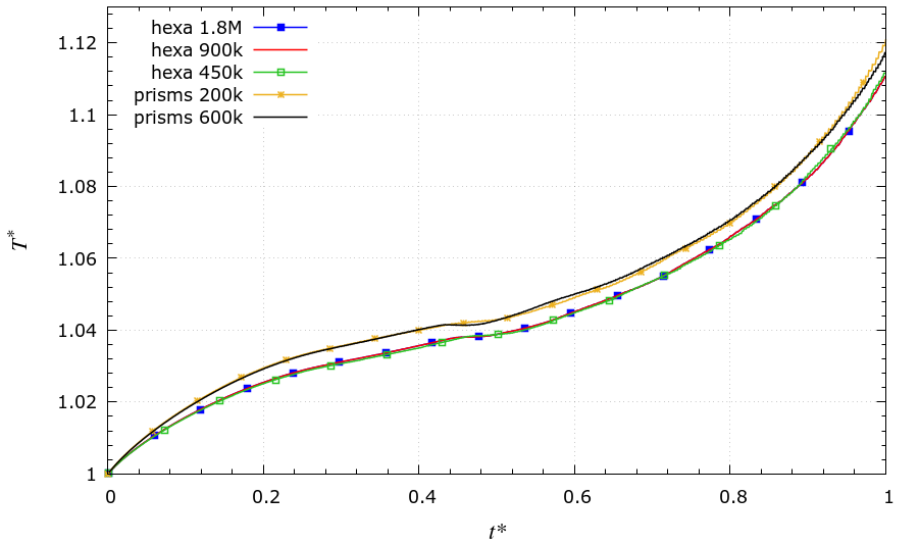


Figure 3: A comparison of air's average temperature evolution through time with different used meshes

### *2.6. Experimental validation of the numerical model*

The CFD results have been compared with the experimental data of Neu & Subrenat [34] under the same operating condition ($U_{pist} = 0.033ms^{-1}$, $CR = 4.8$, $T_{walls} = 293$ K), in view of validating the used numerical model. Both the evolution of average air temperature and pressure and the local air velocity fields were compared, as reported below.

Figure 4 shows a comparison on the evolution of average air temperature ($T^*$) between the numerical and experimental results. The two curves show a similar increasing trend along with the compression process, i.e., the simulated values of average air temperature basically fall within the error margin of the experimental data. Note that this error margin has been determined by considering the uncertainties of the experimental measurement, i.e., the average gap of 10 repeating compression tests performed [34]. The maximum gap between the experimental and numerical results observed at the end of the compression ($t^* = 1$) is below 3 K. It should be noted that the average water temperature does not show any noticeable change over the compression time. Perfect agree-

ment on the evolution of average air pressure can also be observed between the numerical results and experimental data, as shown in Fig. 5. At $t^* = 1$ (final moment), the piston travels 76% of its total length ($L^* = 0.76$), the final pressure reaching $P_f^* = 4.8$.

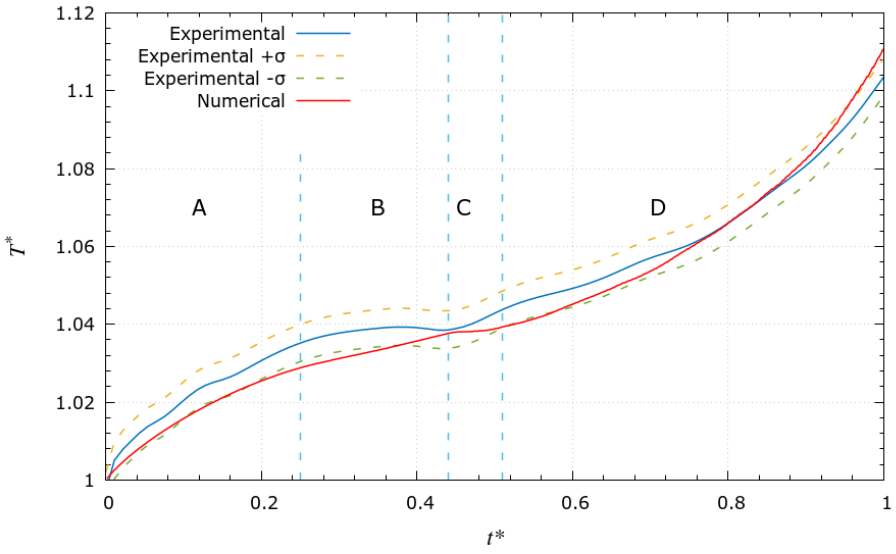


Figure 4: Comparison on the evolution of average air temperature over compression time between numerical results and experimental data from [34].

The air velocity fields obtained by CFD method have also been compared with the PIV results of Neu & Subrenat [34]. Fig. 6 shows a case of established flow structure at $t^* = 0.15$ with very similar axial velocity profiles. In contrast, a transitional flow pattern at $t^* = 0.47$ is presented in Fig. 7, showing clearly the instabilities, the swirling flows and vortices. The flow structure disruption is in a more advanced state in experiments than in simulation. This can be explained by the fact that the average air temperature is a bit higher in experiments with an earlier arrival of the regime transition (cf. Fig. 4). More detailed comparison on the velocity profiles are further presented in the later section. In conclusion, the numerical model used in this study seems to be capable of correctly simulating the flow patterns occurring inside the LP column and the global air temperature evolution during the air compression.

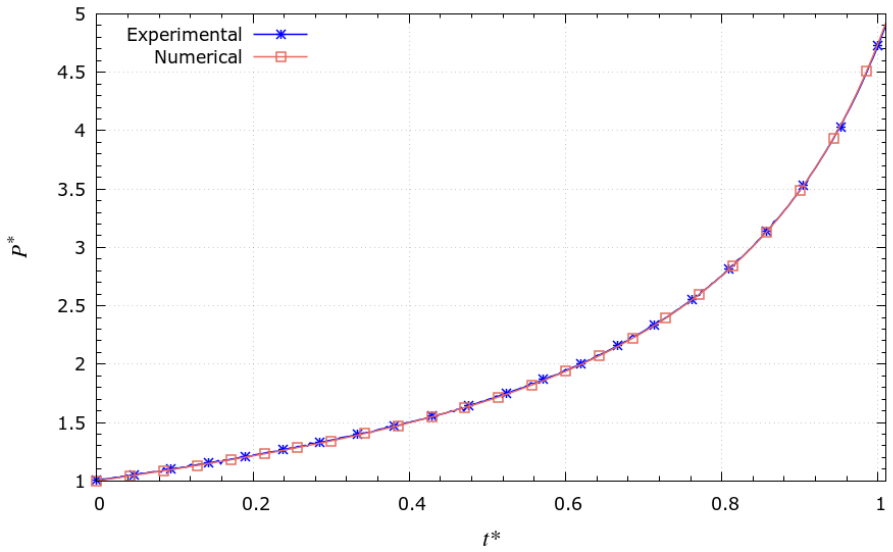


Figure 5: Comparison on the evolution of average air pressure over compression time between numerical results and experimental data from [34].

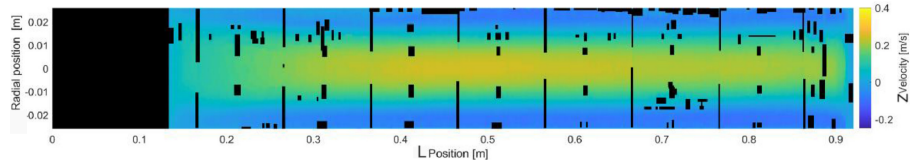


(a) Experimental axial velocity field

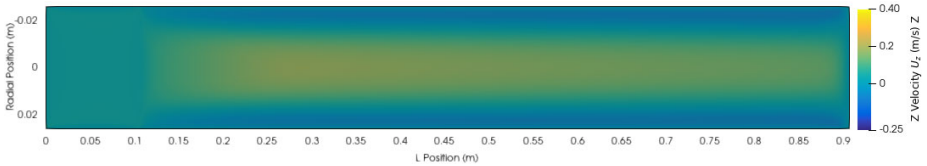


(b) Numerical axial velocity field

Figure 6: Comparison of the axial velocity field between experimental [34] and CFD results at $t^* = 0.15$

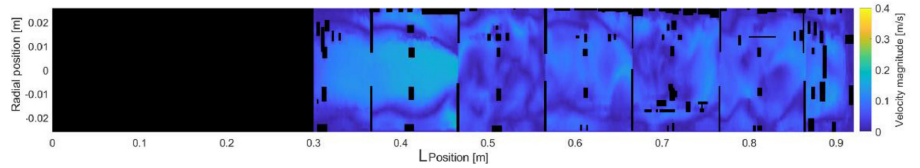


(a) Experimental velocity field (magnitude) [34]

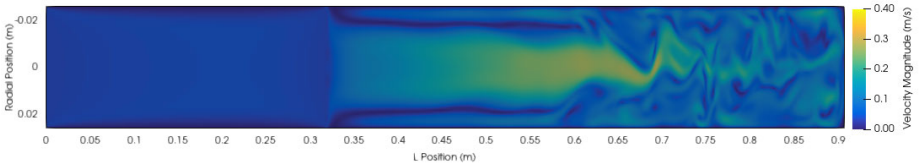


(b) Numerical velocity field (magnitude)

Figure 7: Comparison of the velocity magnitude between experimental [34] and CFD results at $t^* = 0.47$

## 3. Results and discussion

### *3.1. Flow and temperature fields description*

The air average temperature is actually one of the key parameters to indicate the progress of the compression/expansion process by LP. In our case, it goes from $T^*_{ini} = 1$ (293 K) up to $T^*_f = 1.11$ (325.5 K) at $t^*_f = 1$. This temperature increase is far smaller than that for the adiabatic case ($T^*_f = 1.79$), thereby could be considered as a near-isothermal compression. Different stages may be identified in Fig. 4 according to the evolution behavior of the air temperature curve, as described below.

- Stage A from $t^* = 0$ to $t^* = 0.23$ where the temperature increases by about 2 K every second.
- Stage B from $t^* = 0.23$ to $t^* = 0.43$ where the temperature increases slowly but linearly, about 0.5 K per second.
- Stage C from $t^* = 0.43$ to $t^* = 0.52$, lasting about 2 s. The slope of $T^*$ curve decreases and the average air temperature is almost stabilized at $T^* = 1.041$ (305 K) at the inflection point.
- Stage D from $t^* = 0.52$ to $t^* = 1$ where $T^*$ increases more and more rapidly until the end of the compression, reaching $T^*_f = 1.11$ (325.5 K). This time the curve shows a convex shape.

These different stages correspond different flow regimes that occur one after another during the air compression, illustrated by the evolution of air velocity fields shown in Fig. 9.

Firstly, a totally axisymmetric flow structure could be seen for the stage A ($0 < t^* < 0.23$), as shown in Fig. 9a for $t^* = 0.12$ (2.54 s). After a very short start-up period ($t^* < 0.04$) with all ascending air flow initiated by the piston movement, a central uprising air flow surrounded by an peripheral descending flow is established (Fig. 9a). Re-circulation zones connect the rising and falling flows at both the column head (central air deviated to the periphery) and at

the water/air interface (peripheral air carried toward the center). The highest local velocity observed is located closer to the piston front rather than near the cylinder head. The air average temperature at this time ($t^* = 0.12$) is $T^* = 1.017$, 5 K higher than the initial air temperature $T_{ini}$ and the imposed wall temperature $T_{walls}$. A temperature gradient is thereby present, increasing from $T^* = 1$ (293 K) at the surrounding walls to $T^* = 1.024$ (300 K) at $R^* = \pm 0.38$ (the radial position indicated in Fig. 13). The rest of air domain has an almost uniform temperature at $T^* = 1.024$ while the water temperature remains almost unchanged at $T^* = 1$ (Fig. 10a).

Stage B is characterized by both much faster central rising flow (maximum positive $U_z^* = 11.9$) and peripheral falling flow (maximum negative $U_z^* = -8.5$), as shown in Fig. 9b for $t^* = 0.33$ (7.0 s). The highest air velocity is no longer located close to the water/air interface but moves towards the column head where a slightly widened central stream could be seen (Figs. 9b, 8). The global flow structure is maintained but the deformation becomes visible, i.e., small ripples occurring at the interface of rising and falling flows, the axisymmetric feature will thereby be gradually lost. The average air temperature at $t^* = 0.33$ reaches $T^* = 1.034$, about 10 K higher than the $T_{ini}$. The thermal boundary layer close to the column walls is thinner, as shown in Fig. 10b. The column head where the air velocity is the highest has the maximum temperature, reaching $T^* = 1.060$ (310 K). Near the air/water interface, the air at the column center is slightly cooler than that closer to the walls. This is mainly due to the cooling effect of the colder liquid when air recirculates along the water/air interface.

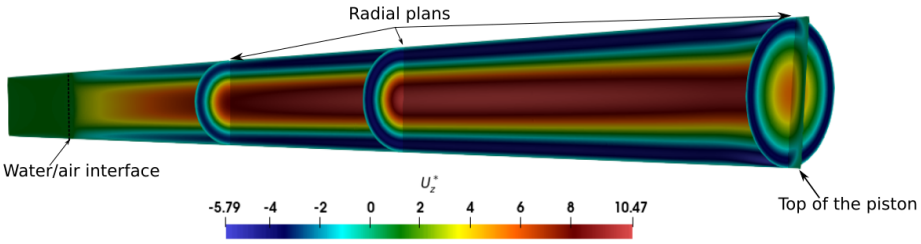


Figure 8: The $U_z^*$ velocity component profile at $t^* = 0.24$; $t = 5s$

The compression enters into the stage C at $t^* = 0.43$ ($L^*_{pist} = 0.327; P^* = 1.5$) which is a short transition regime characterized by the appearance of small instabilities and swirling flows, as shown in Fig. 9c for $t^* = 0.435$ (9.11 s). The positive and negative air velocities recorded in this stage reach $U^*_z = 10$ and $U^*_z = -7.4$, both close to the column head (Fig. 9c). The recorded velocity is slightly lower than that of the previous stage (B). The average air temperature reaches $T^*_{air} = 1.04$, or 12 K higher than the $T_{ini}$. The hottest area ($T^*_{air,ave} = 1.092$; 320 K) is always closer to the column head, in conjunction with the highest velocities. The air flow in the center of the column near the interface is always a bit cooler than that near the walls (Fig. 10c) as explained above. The deformation of the flow structure clearly visible on the velocity field is also reflected by the slightly non-symmetrical temperature field, as shown in Fig. 10c.

This transition stage quickly gives way to the last flow regime (stage D), featured by the breaking up of the main flow structure into a multitude of vortices, and remaining in a chaos state until the end of compression. Despite this chaos, the central flow is still different from the annular flow, in a way that negative velocities are still present closer to the wall, while positive ones are dominant in the center of the column. At the end of the compression ($t^* = 1$; $L^*_{pist} = 0.765$; $P^* = 4.8$), the maximum air velocity reaches $U^*_z = 6$ and $U^*_z = -5$ (Figs. 9d,9e), lower than the ones observed in stages B and C. The average temperature of the air at the end of compression could reach $T^*_{air,ave} = 1.11$ (325.5 K) but local temperature close to the column head could go as high as 360 K (Fig. 10e) . The thermal boundary layer is hardly visible due to the strong turbulence of air flow.

More details about the velocity and temperature fields all along the LP compression can be visualized in the videos provided as supplementary data of this paper. Moreover, the numerical study offers additional assets which enable us to have a deeper analysis of the conjugated flow and heat transfer through local variables evolution (temperature, velocity components, etc.), which is reported in the next subsection.

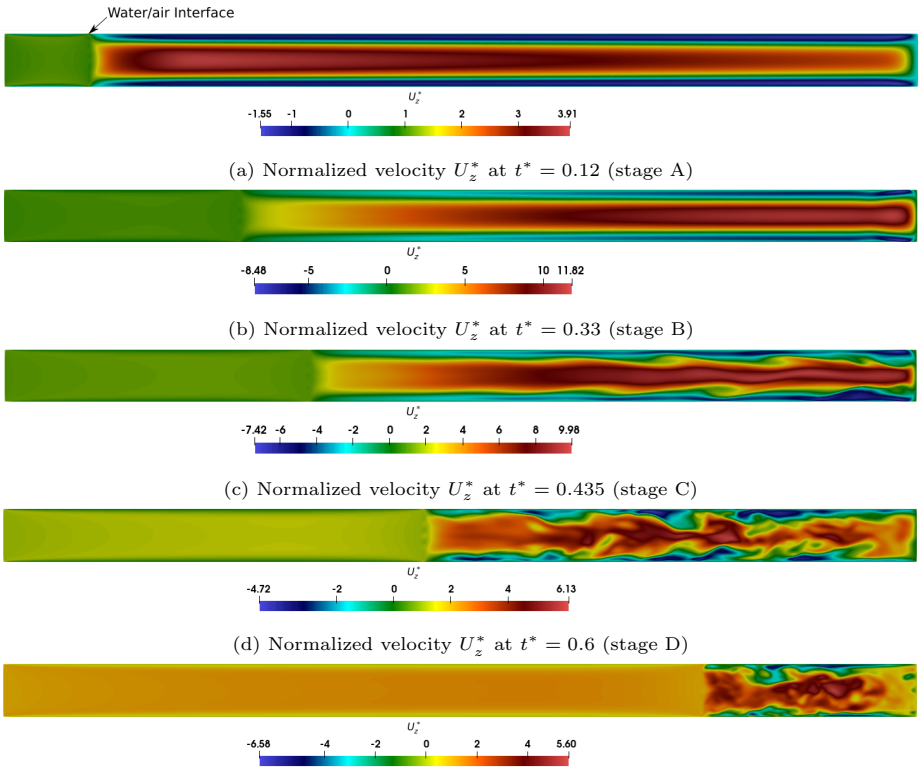


(a) Normalized velocity $U_z^*$ at $t^* = 0.12$ (stage A)

(b) Normalized velocity $U_z^*$ at $t^* = 0.33$ (stage B)

(c) Normalized velocity $U_z^*$ at $t^* = 0.435$ (stage C)

(d) Normalized velocity $U_z^*$ at $t^* = 0.6$ (stage D)

(e) Normalized velocity $U_z^*$ at $t^* = 0.99$ (stage D, end of compression)

Figure 9: Velocity field $U_z^*$ at different compression times

### *3.2. Evolution of velocity and temperature profiles*

The evolution of velocity and temperature profiles at $L_z^* = 0.71$ is further examined in detail in this subsection, as shown in Fig. 12. This longitudinal position in the middle between the piston top and the water/air interface is chosen to represent the air behaviors before the global structure dismantling. When the main flow structure is established (from $t^* = 0.04$ to $t^* = 0.43$), the flow is separated into two parts: one with negative velocity closer to the piston wall and the other with positive velocity in the piston center. For the latter, the velocity profile is totally parabolic, as shown in Fig. 12b. This distinguished flow pattern is generated due to the air temperature difference between the column center and the near-wall region. The cooler and heavier air near the

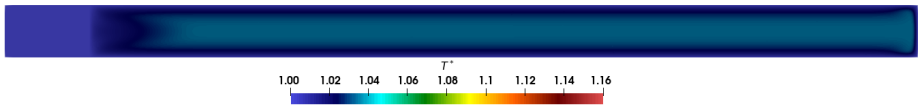


(a) Temperature $T^*$ field at $t^* = 0.12$ (stage A)

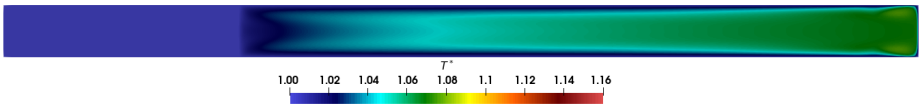


(b) Temperature $T^*$ field at $t^* = 0.33$ (stage B)

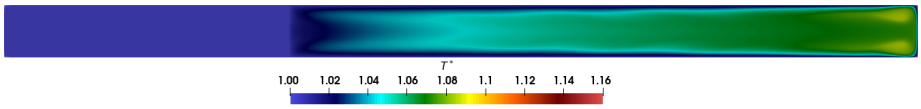


(c) Temperature $T^*$ field at $t^* = 0.435$ (stage C)

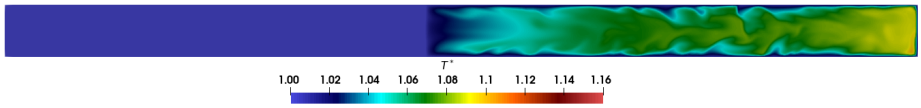


(d) Temperature $T^*$ field at $t^* = 0.6$ (stage D)

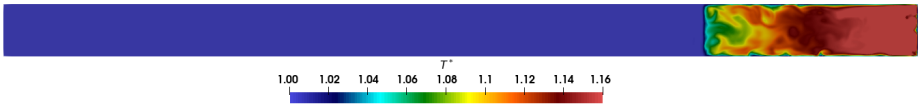


(e) Temperature $T^*$ field at $t^* = 0.99$ (stage D, end of compression)

Figure 10: Dimensionless temperature $T^*$ field at different compression times

wall would descend and form the recirculation.

It can also be observed that the air velocity profile evolves over the compression time, and can go up to more than 10 times the piston speed. The air density also increases with the increasing pressure. Both effects result in the evolution of maximum local Reynolds number of air (as shown in Fig. 11) which can be 20 times higher than the one calculated by Eq. 11 ($Re_{air} = 104$). From Fig. 11, it can be seen that the local $Re_{air}$ grows rapidly in stage A, and remains almost constant at a high level (increased by a factor of 15) in stages B and C. Then it decreases because of the decreased local maximum air velocity at the beginning of stage D, but further increases after $t^* = 0.7$ due to augmented density. This analysis confirms that the definition of average $Re_{air}$ based on the piston advance speed (Eq. 11) and the initial fluid/gas thermophyscial proper-

ties is not relevant to characterize the flow regimes and their transition. The proper turbulent model (LES-WALE in this study) must be employed for the flow modeling during air compression/expansion even if the piston speed is low and the value of average $Re_{air}$ number is small.

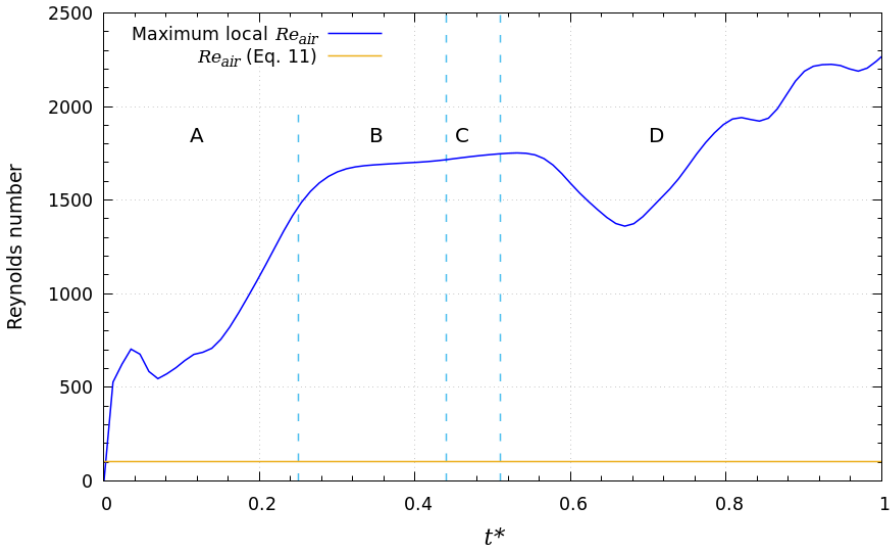


Figure 11: Evolution of the maximum local Reynolds number $Re_{air}$ over compression time, calculated based on $U_{z,max}$ and corresponding air thermophysical properties (Constant $Re_{air}$ (Eq. 11) also introduced for comparison)

The temperature profile also evolves along with the compression time, showing firstly a parabolic shape at the beginning of the compression and then a slight double-humped shape (Fig. 12a). In other words, the lowest air temperature is always at the wall (due to the imposed boundary condition) while the location of the maximum air temperature shifts from the piston center ($R^* = 0$) towards the wall (e.g., $R^* = \pm 0.6$ at $t^* = 0.52$). Fig. 12a also shows that the thickness of thermal boundary layer decreases over time, as already reported in the above subsection. A distinguished feature is that at $t^* = 0.52$ (just 2 s after the flow structure disruption starts), the velocity profile is already chaotic (Fig. 12b) while the temperature profile is globally kept structured and symmetric. This may imply that the flow structure disruption is mainly induced by the local

flow instabilities rather than the temperature instability. Further discussion on this issue can be found in the later subsection.

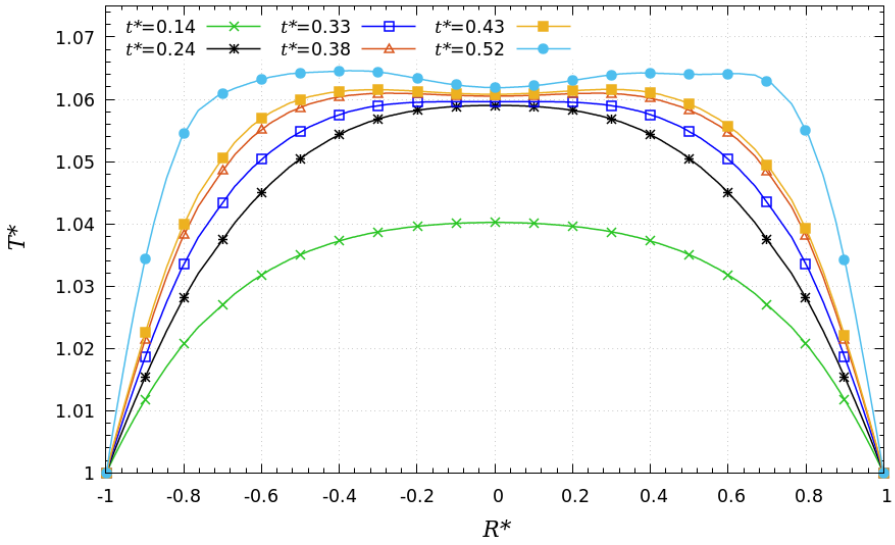


(a) Evolution of temperature $T^*$ profile at $L_z^* = 0.71$

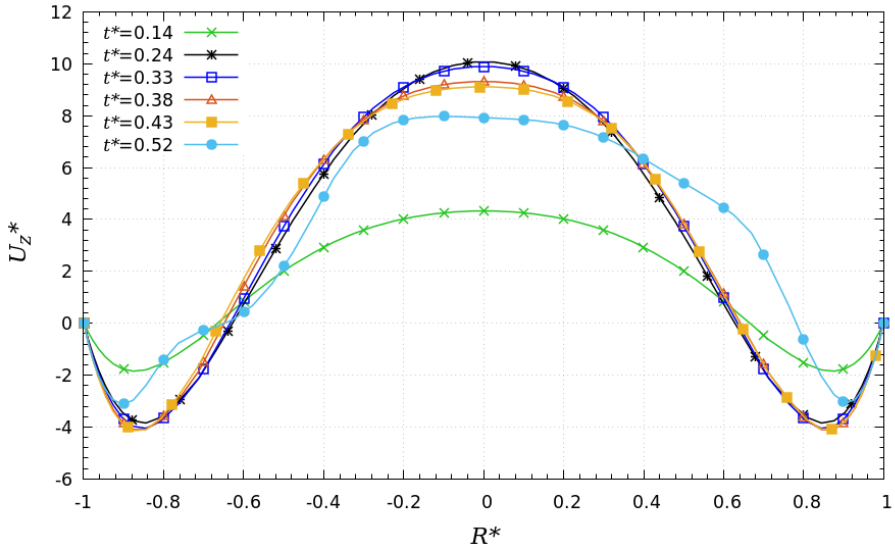


(b) Evolution of velocity $U_z^*$ profile at $L_z^* = 0.71$

Figure 12: Evolution of temperature $T^*$ and velocity $U_z^*$ profiles at $L_z^* = 0.71$ at different $t^*$ moments

*3.3. Local velocities at different radial and longitudinal positions*

The evolution of local air velocities over compression time at different positions of the piston column is further analysed and reported in this subsection, enabling us to better understand the flow mechanisms. The examined radial ($R^*$) and longitudinal ($L_z^*$) positions are indicated in Fig. 13.

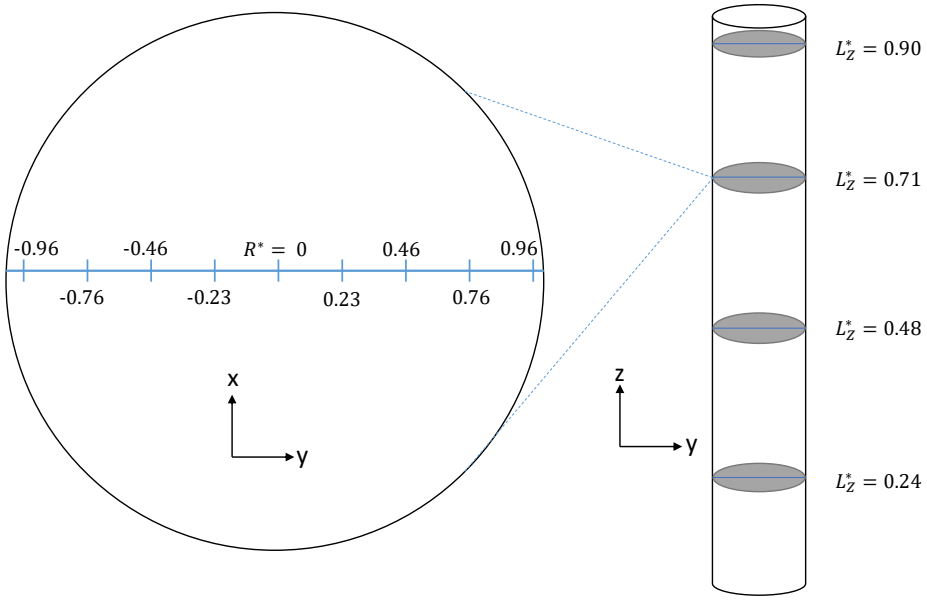


Figure 13: Examined longitudinal ($L_z^*$) and radial ($R^*$) positions

The evolution of $U_z^*$ at $L_z^* = 0.24$ during compression is shown in Fig. 14. The air movement is initiated by the LP advance within a very short time to catch the piston (interface) speed. Starting from $t^* = 0.04\,(< 1s)$, the negative velocities next to the piston wall can be seen, implying the establishment of the above-mentioned rising/falling flow structure such as shown in Fig. 9a. The overlapping of two $U_z^*$ curves at the corresponding (positive and negative) $R^*$ positions indicates the symmetric feature of the velocity profile. The highest velocity of air is in the piston center, which keeps increasing until $t^* = 0.14(\sim 3s)$ and then continuously decreases until the arriving of water at $t^* = 0.31$.

Fig. 15 shows the $U_z^*$ curves as a function of $t^*$ at $L_z^* = 0.48$. Similarly, the air velocity first increases till $t^* = 0.2\,(\sim 4.2s)$ and the maximum velocity

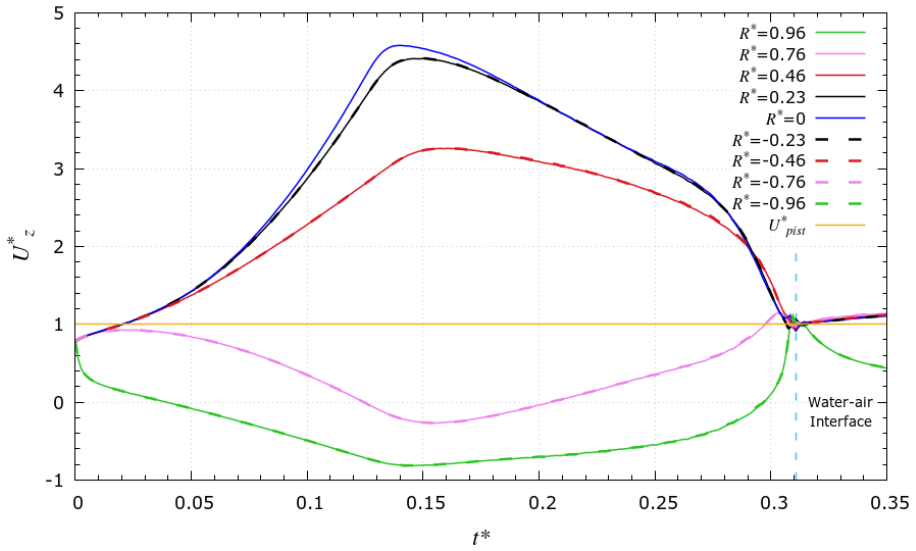


Figure 14: $U_z^*$ vs. $t^*$ at $L_z^* = 0.24$

observed is about 8 times the $U_{pist}^*$. The flow structure is axisymmetric until the appearance of small ripples or wavelets close to the piston wall, reflected on Fig. 15 as the no longer overlapping $U_z^*$ curves at corresponding $R^*$ positions. More fluctuations can be seen before the arrival of water at $L_z^* = 0.48$.

Similar trend may be observed on Fig. 16 for $L_z^* = 0.71$, but higher $U_z^*$ values have been registered ($> 10$ times the $U_{pist}^*$). Especially, a sudden falling (or rising) of $U_z^*$ curves could be identified between $t^* = 0.43$ and $t^* = 0.52$, the period corresponding to the transition stage of the air compression. After $t^* = 0.52$, the $U_z^*$ curves become highly fluctuated, indicating the turbulent pattern of air flow. An additional analysis of the radial velocity component $U_x^*$ shows that before $t^* = 0.36$ this component is almost null (Fig. 17). Since then, the negative values of $U_x^*$ indicate the appearance of ripples and wavelets, and from a certain moment, the sudden disruption of the global flow structure occurs.

Almost the same dynamics and transition stages as those for $L_z^* = 0.71$ can be observed on Fig. 18 for $L_z^* = 0.90$. The maximum positive velocity

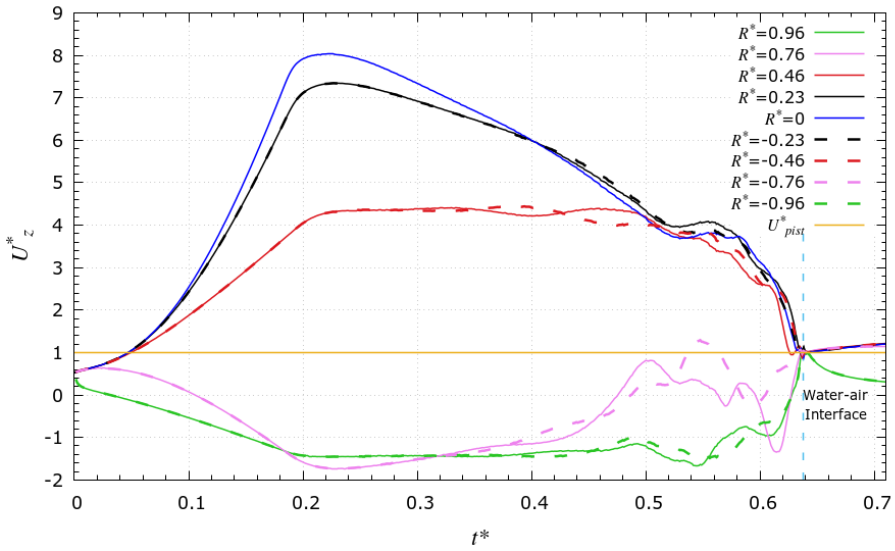


Figure 15: $U_z^*$ vs. $t^*$ at $L_z^* = 0.48$

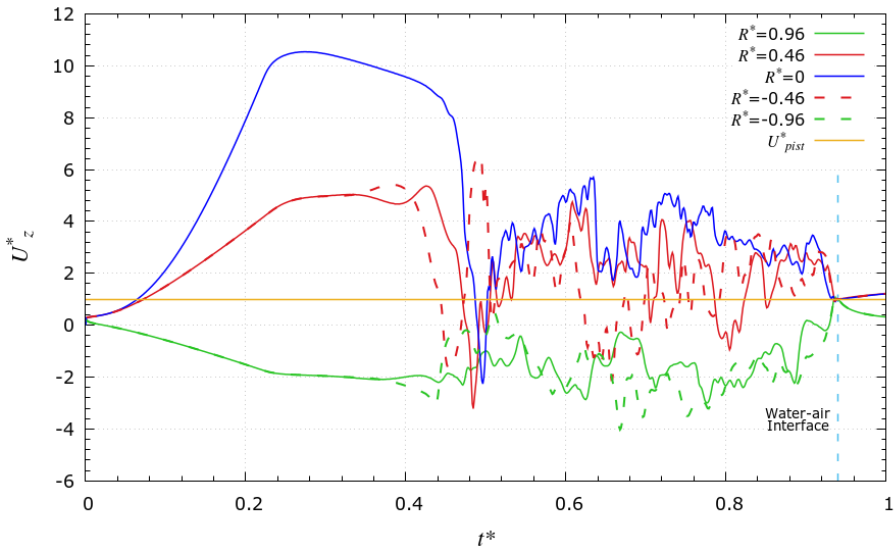


Figure 16: Local velocity $U_z^*$ vs. $t^*$ at $L_z^* = 0.71$

($U_z^* \sim 11.5$ at $t^* = 0.28$) is registered in the piston center $R^* = 0$, while negative axial velocities are dominant at $R^* = \pm 0.96$. An additional comparison with the experimental results of Neu & Subrenat [34] on the $U_z^*$ curves ($R^* = 0$ and 0.96)

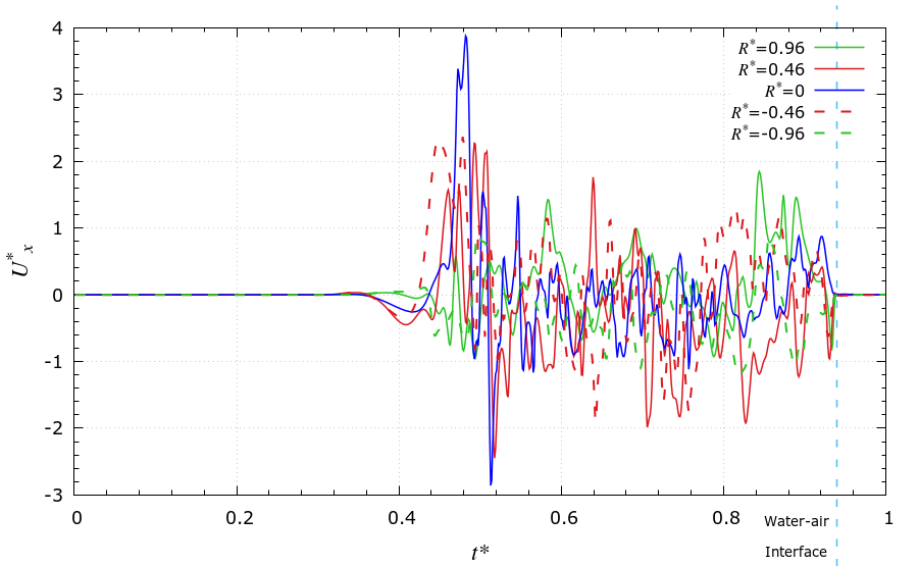


Figure 17: Local velocity $U_x^*$ vs. $t^*$ at $L_z^* = 0.71$

is shown in Fig. 18 at $L_z^* = 0.90$. Good agreement between the experimental and CFD results can be found for the time period $0 < t^* < 0.31$ $(0 - 6.5s)$ with globally matched evolution trend and maximum values, and for $t^* > 0.52$ when the chaotic turbulent flow pattern can be identified. Nevertheless, in the experimental results, the $U_z^*$ suddenly falls/rises at $t^* = 0.37$, about 1.25 s earlier than that of the numerical results. This earlier arrival of flow regime transition, already mentioned when discussing the Fig. 4 in section 2, can be derived from various simplifications (e.g., solid piston instead of LP in experiments, isothermal wall in CFD simulation, etc.) and uncertainties (PIV measurement, VOF-LES model, etc.) of both methods. Moreover, the small roughness or irregularities of the piston column experimentally tested may favor the flow structure disruption. But in general, the CFD model and associated parameters are again verified to be adequate to describe the flow thermohydrodynamics of air compression inside the LP column.

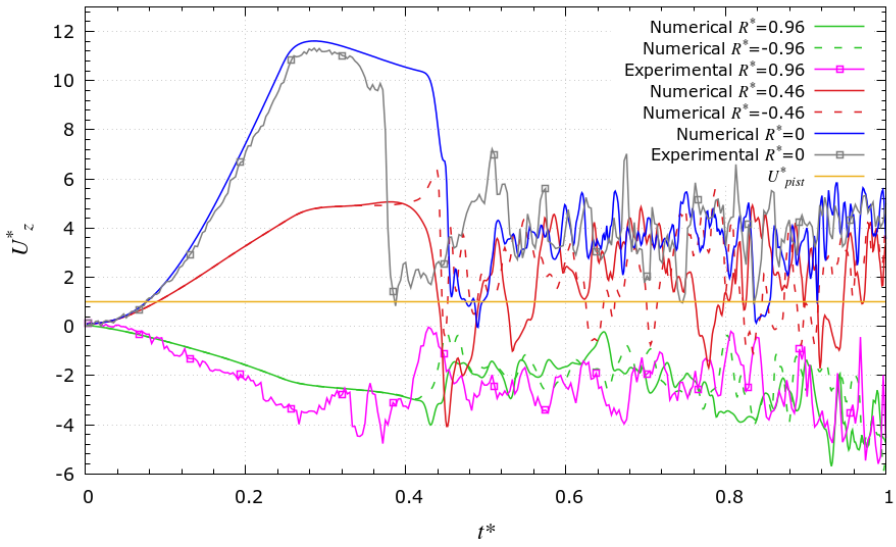


Figure 18: Comparison between experimental and CFD results on $U_z^*$ at $L_z^* = 0.90$

## 4. Further discussions

### *4.1. Origin of flow structure dismantling*

The dismantling from a structured flow to a chaotic one, which occurs almost instantly, is a key phenomenon in understanding the flow regime transition of LP air compression process. The available experimental techniques are either difficult to implement or still inadequate to precisely monitor the sudden change of flow behaviors within such a short period of time. In complement, the CFD simulation and post-treatment could allow a better tracking of the flow, providing additional insights to reveal the origin of this flow structure disruption. To do this, all the velocity components ($U_x^*$, $U_y^*$, $U_z^*$) of the flow have to be closely examined to locate the position and the time of the first structure deformation.

From Fig 19, it can be seen that the first perturbation on $U_z^*$ occurs at $t^* = 0.39$ (8.2 s) at about $L_z^* = 0.9$, where the maximum velocities and the highest local temperature are located. The origin of this perturbation could be the instabilities generated by the high velocity gradients and the shear stress at the interface between the ascending and descending flows (light blue zones in Fig.

19b). The perturbation is then spread in both directions towards the water/air interface and the column head (Fig. 19c), evidenced by the ripple shape of flow structure as shown in Fig. 9d. Despite the velocity profile asymmetry, the integral flow structure is still kept for a while (about 1 s), until the accumulation of perturbations triggers the sudden structure dismantling at $t^* = 0.43$. Further evidences are still needed to verify whether this flow disruption phenomenon is caused by Kelvin-Helmotz instability [34].

*4.2. Evolution of air flow rate at different positions of the piston column*

Neu & Subrenat [34] has proposed a relation (Eq. 12) to estimate the evolution of air volume flow rate at a certain position of the piston column, by considering a linear increase of the air pressure due to the volume reduction of the air domain.

$$Q_z(t) = Q_{pist} \frac{L_{ini} - L_z}{L_{ini} - L_{pist}(t)} \tag{12}$$

where $Q_z(t)$ is the total air flow rate through the cross-section at $L_z$ height, $Q_{pist}$ ($7 \times 10^{-5} m^3 s^{-1}$) is the air flow rate imposed by the movement of the water.

The normalized air flow rate $Q_z^*(t)$ can be expressed as follows (Eq. 13):

$$Q_z^*(t) = \frac{Q_z(t)}{Q_{pist}} = \frac{1 - L_z^*}{1 - L_{pist}^*(t)} \tag{13}$$

As presented in the previous sections, the flow structure undergoes several stages and both the positive and negative axial velocities could exist. As a result, the flow rate studied here is the sum of the negative and positive values, while the radial components are neglected. Fig. 20 shows a comparison on the evolution of air flow rate over compression time at different positions between the relation-estimated results and CFD results. It can be observed that the prediction and simulation results are in good agreement at the beginning of compression at all $L_z^*$ positions. A noticeable departure can be found for $L_z^* = 0.71$ and $L_z^* = 0.90$, due to the established "central ascending-peripheral descending" air flow structure. When the flow regime transition is finished and turbulent

flow established at $t^* = 0.52$, the predicted and simulated curves show again a similar increasing profile.

Based on this comparison, it can be seen that the Neu & Subrenat relation (Eq. 13) is better adapted for small $L_z^*$ positions and small $t^*$ values, but discrepancy might exist for large $L_z^*$ positions especially before the total dismantling of the main flow structure.

### *4.3. Effect of piston speed on temperature evolution*

To better determine the effect of the piston speed on the flow and heat transfer behaviors of LP compression process, simulations have been performed by increasing or decreasing threefold the initial $U_{pist}$. The parameters of the additional tested cases are listed in Table. 6.

| Cases | $U_{pist}$ $(ms^{-1})$ | $t_f$ $(s)$ | $V_f$ $(m^3)$ | $T_{air,ave,f}$ $(K)$ |
|---|---|---|---|---|
| Slow | 0.01 | 69.3 | $1.46 \times 10^{-3}$ | 306.6 |
| Reference | 0.033 | 21 | $1.46 \times 10^{-3}$ | 325.7 |
| Fast | 0.1 | 6.93 | $1.46 \times 10^{-3}$ | 356.9 |

Table 6: Parameters of the three studied cases on the effect of piston speed

Figure 21 shows the evolution of average air temperature for three studied cases, all of them showing the increasing trend with $t^*$. The four stages and corresponding flow patterns are still present in the other tested cases, but their durations and the occurring moments are different. It can be seen from Fig. 21 that the higher the piston speed, the faster the air temperature increases and the higher the final temperature. For the fast compression case ($U_{pist} = 0.1\, ms^{-1}$), the final temperature reaches $T_{air}^* = 1.22\,(356.9\, K)$, 50.3 K higher than that of the slow compression case ($U_{pist} = 0.01\, ms^{-1}$; $T_{air}^* = 1.045$). Without efficient heat removal measure, the departure from the isothermal compression at fast piston speed condition would result in the reduced compression efficiency as well as the RTE of the CAES system. The interest of LP is thereby partially lost. Nevertheless, the amount of energy stored or discharged within a certain period

of time might be less influenced (or even increased) because a higher number of charging/discharging cycles could be performed. Further system level analysis on the cyclic operations of LP-based CAES system is interesting by taking both the RTE and the storage capacity into account.

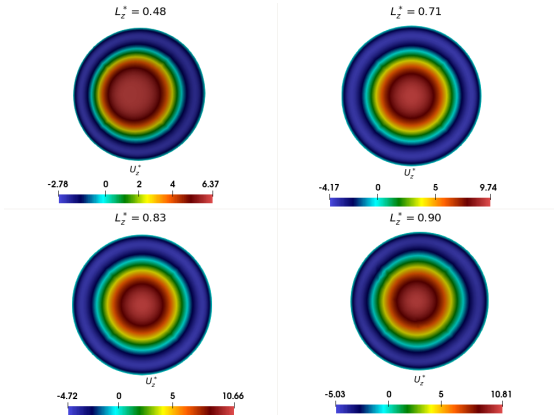


(a) $t^* = 0.37$ (before disruption)

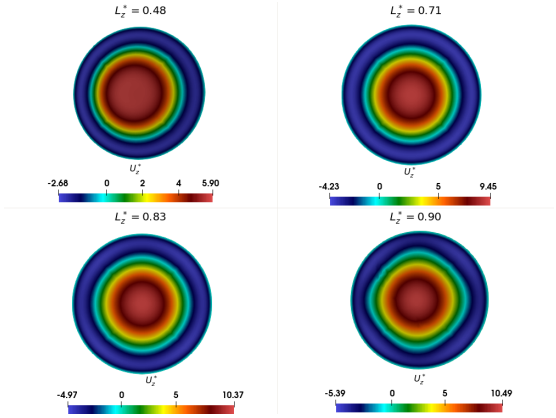


(b) $t^* = 0.39$ (at first apparition of disruption)

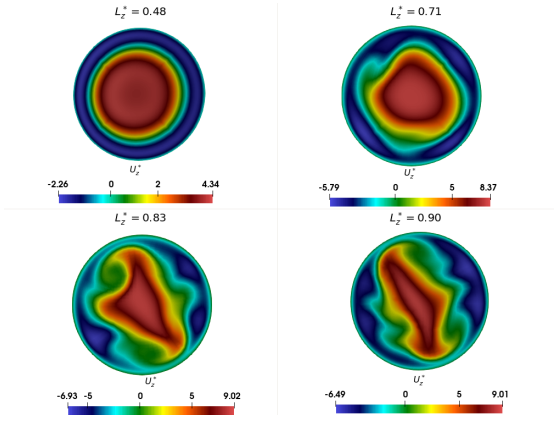


(c) $t^* = 0.52$ (after disruption)

Figure 19: $U_z$ cartography at different radial sections ($L_z^* = 0.48; 0.71; 0.83$ and $0.90$) during the flow structure disruption/dismantling

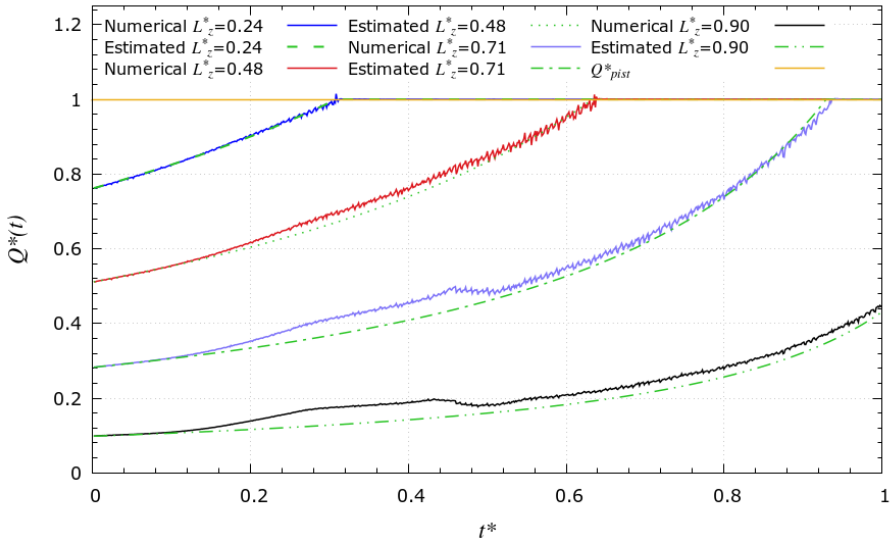


Figure 20: Evolution of air flow rate over compression time at different axial positions of the LP column

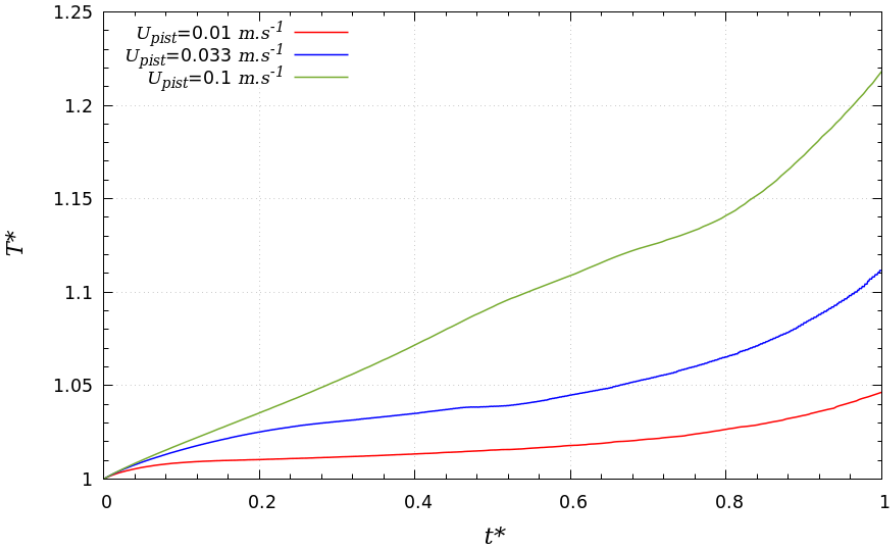


Figure 21: Evolution of average air temperature over compression time for different piston speeds

## 5. Conclusion and prospects

A full 3D CFD model for LP compressor using the FVM coupled with the VOF method for interface tracking has been developed in this study and validated by the existing experimental data-sets. The fluid flow dynamics and the coupled heat transfer behaviors inside the LP column during air compression has been simulated and analysed in detail for the first time, enabling a better understanding of the flow regimes and their transition. Main findings of this study can be summarized as follows.

- Different compression stages can be identified, each stage having its distinguished flow pattern and heat transfer characteristics. An axisymmetric flow structure with ascending flow in the column center and descending one close to the piston walls is established during the first seconds of compression. The local air velocity could vary between $-8.5 < U_z^* < 12$, implying that the conventionally-used global Reynolds number based on the piston speed is not the appropriate parameter to characterize the flow regimes and their transition.

- The first flow perturbation occurs at the location with the highest velocity gradients ($L_z^* = 0.90$) and then propagates towards both ends, resulting in the ripple shape of the main flow structure. The flow instabilities due to the high shear stress and frictions between the central rising and peripheral falling streams might be the cause of this flow structure disruption.

- The transition stage for the flow structure dismantling is relatively fast, occurring at about $t^* = 0.43$ and lasting about 2 s. After that the flow becomes totally chaotic with rapidly increasing air temperature, reaching $T_{ave}^* = 1.11$ (325.5 K) at the end of the compression. This temperature rise is far smaller than that of adiabatic compression ($T^* = 1.79$; 524.5 K), confirming the interests of LP to approach the near-isothermal CAES.

- The fast piston speed would result in the elevated final air temperature and departure from the isothermal compression condition. Efficient heat

removal measures are especially needed for LP compressors working on relatively high piston speed.

As prospects, systematic parametric studies (piston speed, CR and $L/D$ ratios, external environment, etc.) would help reveal the separate effect of each factor as well as their combined influences on the compression efficiency. Deeper analyses and understanding of the physical phenomena are still needed in view of proposing adapted analytical physical models to describe and predict the flow regimes and the coupled heat transfer characteristics. The wall effect on the efficiency of the LP operation needs to be evaluated through a coupling of the fluid domain with a solid wall with a certain thickness. The simulation and analysis of a complete compression-storage-expansion cycle to quantify the RTE of the CAES system using LP is our on-going work. Finally, a topology optimization method is expected to be developed to determine the optimal column geometries and operating conditions with the aim of better approaching the isothermal-CAES for the energy storage.

**Acknowledgement**

This work is supported by the French Association Nationale de la Recherche et de la Technologie (ANRT) under the CIFRE program No. 2017/1100. A part of this work was performed using computing resources of CCIPL (Centre de Calcul Intensif des Pays de la Loire), France.

**References**

[1] I. E. Agency, Renewables – Global Energy Review 2021 – Analysis, Tech. rep., International Energy Agency : IEA (2021).
URL `https://www.iea.org/reports/global-energy-review-2021/renewables`

[2] P. Seferlis, P. S. Varbanov, A. I. Papadopoulos, H. H. Chin, J. J. Klemeš, Sustainable design, integration, and operation for energy high-performance

process systems, Energy 224 (2021) 120158. doi:10.1016/J.ENERGY.2021.120158.

[3] U. Pelay, L. Luo, Y. Fan, D. Stitou, C. Castelain, Integration of a thermochemical energy storage system in a Rankine cycle driven by concentrating solar power: Energy and exergy analyses, Energy 167 (2019) 498–510. doi:10.1016/j.energy.2018.10.163.

[4] N. McIlwaine, A. M. Foley, D. J. Morrow, D. Al Kez, C. Zhang, X. Lu, R. J. Best, A state-of-the-art techno-economic review of distributed and embedded energy storage for energy systems, Energy 229 (2021) 120461. doi:10.1016/J.ENERGY.2021.120461.

[5] D. Fan, Y. Ren, Q. Feng, Y. Liu, Z. Wang, J. Lin, Restoration of smart grids: Current status, challenges, and opportunities, Renewable and Sustainable Energy Reviews 143 (2021) 110909. doi:10.1016/J.RSER.2021.110909.

[6] J. Bai, W. Wei, L. Chen, S. Mei, Modeling and dispatch of advanced adiabatic compressed air energy storage under wide operating range in distribution systems with renewable generation, Energy 206 (2020) 118051. doi:10.1016/J.ENERGY.2020.118051.

[7] M. Dooner, J. Wang, Compressed-Air Energy Storage, Future Energy: Improved, Sustainable and Clean Options for Our Planet (2020) 279–312doi:10.1016/B978-0-08-102886-5.00014-1.

[8] X. Luo, J. Wang, M. Dooner, J. Clarke, Overview of current development in electrical energy storage technologies and the application potential in power system operation, Applied Energy 137 (2015) 511–536. doi:10.1016/j.apenergy.2014.09.081.

[9] M. Budt, D. Wolf, R. Span, J. Yan, A review on compressed air energy storage: Basic principles, past milestones and recent developments, Applied Energy 170 (2016) 250–268. doi:10.1016/j.apenergy.2016.02.108.

[10] A. G. Olabi, T. Wilberforce, M. Ramadan, M. A. Abdelkareem, A. H. Alami, Compressed air energy storage systems: Components and operating parameters – A review, Journal of Energy Storage 34 (2021) 102000. doi:10.1016/J.EST.2020.102000.

[11] Q. Zhou, D. Du, C. Lu, Q. He, W. Liu, A review of thermal energy storage in compressed air energy storage system, Energy 188 (2019) 115993. doi:10.1016/j.energy.2019.115993.

[12] E. M. Gouda, Y. Fan, M. Benaouicha, T. Neu, L. Luo, Review on Liquid Piston technology for compressed air energy storage, Journal of Energy Storage 43C (2021) 103111. doi:10.1016/J.EST.2021.103111.

[13] J. D. Van de Ven, P. Y. Li, Liquid piston gas compression, Applied Energy 86 (10) (2009) 2183–2191. doi:10.1016/j.apenergy.2008.12.001.

[14] T. Neu, C. Solliec, B. dos Santos Piccoli, Experimental study of convective heat transfer during liquid piston compressions applied to near isothermal underwater compressed-air energy storage, Journal of Energy Storage 32 (2020) 101827. doi:10.1016/j.est.2020.101827.

[15] T. NEU, Device And Method For Converting And Storing Electric Energy In The Form Of Compressed Air (12 2016).
URL https://patentscope.wipo.int/search/en/detail.jsf?docId=WO2016193322

[16] O. Maisonnave, L. Moreau, R. Aubrée, M. F. Benkhoris, T. Neu, D. Guyomarc'h, Optimal energy management of an underwater compressed air energy storage station using pumping systems, Energy Conversion and Management 165 (2018) 771–782. doi:10.1016/j.enconman.2018.04.007.

[17] A. Odukomaiya, A. Abu-Heiba, K. R. Gluesenkamp, O. Abdelaziz, R. K. Jackson, C. Daniel, S. Graham, A. M. Momen, Thermal analysis of near-isothermal compressed gas energy storage system, Applied Energy 179 (2016) 948–960. doi:10.1016/j.apenergy.2016.07.059.

[18] C. Zhang, P. Y. Li, J. D. Van De Ven, T. W. Simon, Design analysis of a liquid-piston compression chamber with application to compressed air energy storage, Applied Thermal Engineering 101 (2016) 704–709. doi:10.1016/j.applthermaleng.2016.01.082.

[19] V. C. Patil, P. I. Ro, Modeling of liquid-piston based design for isothermal ocean compressed air energy storage system, Journal of Energy Storage 31 (2020) 101449. doi:10.1016/j.est.2020.101449.

[20] W. Q. Xu, Z. Y. Du, X. S. Wang, M. L. Cai, Y. Shi, H. J. Yan, J. Wang, Air Compression Method Based on Isothermal Piston Heat Exchange, Beijing Ligong Daxue Xuebao/Transaction of Beijing Institute of Technology 40 (5) (2020) 501–506. doi:10.15918/j.tbit1001-0645.2018.458.

[21] V. C. Patil, P. Acharya, P. I. Ro, Experimental investigation of heat transfer in liquid piston compressor, Applied Thermal Engineering 146 (2019) 169–179. doi:10.1016/j.applthermaleng.2018.09.121.

[22] C. Qin, E. Loth, P. Y. Li, T. Simon, J. Van De Ven, Spray-cooling concept for wind-based compressed air energy storage, Journal of Renewable and Sustainable Energy 6 (4) (2014) 043125. doi:10.1063/1.4893434.

[23] J. Wieberdink, P. Y. Li, T. W. Simon, J. D. Van de Ven, Effects of porous media insert on the efficiency and power density of a high pressure (210 bar) liquid piston air compressor/expander : An experimental study, Applied Energy 212 (2018) 1025–1037. doi:10.1016/j.apenergy.2017.12.093.

[24] E. M. Gouda, M. Benaouicha, T. Neu, L. Luo, Y. Fan, Méthode VOF pour la simulation numérique de l'écoulement de l'air comprimé et du transfert thermique associé dans un piston liquide, in: 24e Congrès Français de Mécanique (CFM2019), Brest, 2019, pp. 220–226.

[25] C. Zhang, M. Saadat, P. Y. Li, T. W. Simon, Heat transfer in a long, thin tube section of an air compressor: An empirical correlation from CFD and a thermodynamic modeling, in: ASME International Mechanical Engineering

Congress and Exposition, Proceedings (IMECE), Vol. 7, 2012, pp. 1601–1607. doi:10.1115/IMECE2012-86673.

[26] C. Zhang, J. H. Wieberdink, F. A. Shirazi, B. Yan, T. W. Simon, P. Y. Li, Numerical investigation of metal-foam filled liquid piston compressor using a two-energy equation formulation based on experimentally validated models, in: ASME International Mechanical Engineering Congress and Exposition, Proceedings (IMECE), Vol. 8 B, ASME, 2013, p. V08BT09A045. doi:10.1115/IMECE2013-63854.

[27] J. Coetzee, M. Schober, M. Deichsel, E. Schlücker, Computational fluid dynamics simulation and experimental validation of heat transfer in liquid piston compressors, in: 12th International Conference on Heat Transfer, Fluid Mechanics and Thermodynamics, HEFAT, 2016, pp. 511–516.

[28] M. Mutlu, M. Kiliç, Effects of piston speed, compression ratio and cylinder geometry on system performance of a liquid piston, Thermal Science 20 (5) (2016) 1953–1961. doi:10.2298/TSCI140926146M.

[29] R. K. Shah, D. P. Sekulic, Classification of Heat Exchangers, in: Fundamentals of Heat Exchanger Design, Wiley Online Books, John Wiley & Sons, Inc., 2003, pp. 1–77. doi:https://doi.org/10.1002/9780470172605.ch1.

[30] J. Tuhovcak, J. Hejčík, M. Jícha, Modelling fluid flow in a reciprocating compressor, EPJ Web of Conferences 92 (2015) 2100. doi:10.1051/epjconf/20159202100.

[31] E. M. Gouda, M. Benaouicha, T. Neu, P. Vergnol, F. Yilin, L. Luo, 2D versus 3D numerical modeling of flow and heat transfer in a liquid piston air compressor, in: ICNAAM 2021 19th International Conference Of Numerical Analysis And Applied Mathematics, Rhodes, Greece, 2021.

[32] C. Zhang, B. Yan, J. H. Wieberdink, P. Y. Li, J. D. Van de Ven, E. Loth, T. W. Simon, Thermal analysis of a compressor for application to Com-

pressed Air Energy Storage, Applied Thermal Engineering 73 (2) (2014) 1402–1411. doi:10.1016/j.applthermaleng.2014.08.014.

[33] C. Li, H. Wang, X. He, Y. Zhang, Experimental and thermodynamic investigation on isothermal performance of large-scaled liquid piston, Energy 249 (2022) 123731. doi:10.1016/J.ENERGY.2022.123731.

[34] T. Neu, A. Subrenat, Experimental investigation of internal air flow during slow piston compression into isothermal compressed air energy storage, Journal of Energy Storage 38 (2021) 102532. doi:10.1016/j.est.2021.102532.

[35] C. Piya, I. Sircar, J. D. Van de Ven, D. J. Olinger, Numerical Modeling of Liquid Piston Gas Compression, in: Heat Transfer, Fluid Flows, and Thermal Systems, Vol. 9, ASMEDC, 2009, pp. 507–517. doi:10.1115/IMECE2009-10621.

[36] C. Zhang, F. A. Shirazi, B. Yan, T. W. Simon, P. Y. Li, J. D. Van de Ven, Design of an interrupted-plate heat exchanger used in a liquid-piston compression chamber for compressed air energy storage, in: ASME 2013 Heat Transfer Summer Conf. Collocated with the ASME 2013 7th Int. Conf. on Energy Sustainability and the ASME 2013 11th Int. Conf. on Fuel Cell Science, Engineering and Technology, HT 2013, Vol. 2, ASME, 2013, p. V002T04A002. doi:10.1115/HT2013-17484.

[37] C. Zhang, J. H. Wieberdink, T. W. Simon, P. Y. Li, J. D. Van de Ven, E. Loth, Numerical analysis of heat exchangers used in a liquid piston compressor using a one-dimensional model with an embedded two-dimensional submodel, in: ASME International Mechanical Engineering Congress and Exposition, Proceedings (IMECE), Vol. 8A, ASME, 2014, p. V08AT10A095. doi:10.1115/IMECE2014-38567.

[38] C. Qin, E. Loth, Liquid piston compression efficiency with droplet heat transfer, Applied Energy 114 (2014) 539–550. doi:10.1016/j.apenergy.2013.10.005.

[39] H. Zhou, P. Dong, S. Zhao, M. Geng, Y. Guo, Y. Wang, Interrupted plate porous media design for ionic liquid-type liquid piston hydrogen compressor and analysis of the effect on compression efficiency, Journal of Energy Storage 51 (2022) 104410. doi:10.1016/J.EST.2022.104410.

[40] T. Neu, Etude expérimentale et modélisation de la compression quasi isotherme d'air pour le stockage d'énergie en mer, Ph.D. thesis, Ecole nationale supérieure Mines-Télécom Atlantique (6 2017).
URL https://tel.archives-ouvertes.fr/tel-01674267/

[41] C. W. Hirt, B. D. Nichols, Volume of fluid (VOF) method for the dynamics of free boundaries, Journal of Computational Physics 39 (1) (1981) 201–225. doi:10.1016/0021-9991(81)90145-5.

[42] S. Mirjalili, S. S. Jain, M. Dodd, Interface-capturing methods for two-phase flows: An overview and recent developments, Center for Turbulence Research Annual Research Briefs 2017 (117-135) (2017) 13.

[43] The OpenFOAM Foundation, OpenFOAM — Free CFD Software — The OpenFOAM Foundation.
URL https://openfoam.org/

[44] F. Nicoud, F. Ducros, Subgrid-Scale Stress Modelling Based on the Square of the Velocity Gradient Tensor, Flow, Turbulence and Combustion 62 (3) (1999) 183–200. doi:10.1023/A:1009995426001.

[45] J. H. Ferziger, M. Perić, Computational Methods for Fluid Dynamics, Computational Methods for Fluid Dynamicsdoi:10.1007/978-3-642-56026-2.

[46] R. I. Issa, Solution of the implicitly discretised fluid flow equations by operator-splitting, Journal of Computational Physics 62 (1) (1986) 40–65. doi:10.1016/0021-9991(86)90099-9.

[47] S. S. Deshpande, L. Anumolu, M. F. Trujillo, Evaluating the performance of the two-phase flow solver interFoam, Computational Science & Discovery 5 (1) (2012) 014016. doi:10.1088/1749-4699/5/1/014016.

[48] J. Roenby, H. Bredmose, H. Jasak, A computational method for sharp interface advection, Royal Society Open Science 3 (11). doi:10.1098/RSOS.160405.